ChemElectroChem

Research Article
doi.org/10.1002/celc.202200929

Chemistry Europe
European Chemical Societies Publishing

www.chemelectrochem.org

Effect of Ti-Substitution on the Properties of P3 Structure $Na_{2/3}Mn_{0.8}Li_{0.2}O_2$ Showing a Ribbon Superlattice

Stephanie F. Linnell,[a, b] Eun Jeong Kim,[a, b] Le Anh Ma,[c] Aaron B. Naden,[a] John T. S. Irvine,[a, b] Reza Younesi,[c] Laurent C. Duda,[d] and A. Robert Armstrong*[a, b]

Oxygen anion redox offers an effective strategy to enhance the energy density of layered oxide positive electrodes for sodium- and lithium-ion batteries. However, lattice oxygen loss and irreversible structural transformations over the first cycle may result in large voltage hysteresis, thereby impeding practical application. Herein, ribbon superstructure ordering of Li/transition-metal-ions was applied to suppress the voltage hysteresis combined with Ti-substitution to improve the cycling stability for P3-$Na_{0.67}Li_{0.2}Ti_{0.15}Mn_{0.65}O_2$. When both cation and anion redox reactions are utilized, $Na_{0.67}Li_{0.2}Ti_{0.15}Mn_{0.65}O_2$ delivers a reversible capacity of 172 mA h g^{-1} after 25 cycles at 10 mA g^{-1} between 1.6–4.4 V *vs.* Na^+/Na. Ex-situ X-ray diffraction data reveal that the ribbon superstructure is retained with negligible unit cell volume expansion/contraction upon sodiation/desodiation. The performance as a positive electrode for Li-ion batteries was also evaluated and P3-$Na_{0.67}Li_{0.2}Ti_{0.15}Mn_{0.65}O_2$ delivers a reversible capacity of 180 mA h g^{-1} after 25 cycles at 10 mA g^{-1} when cycled vs. Li^+/Li between 2.0–4.8 V.

Introduction

Conventional oxide-based intercalation positive electrode materials for lithium- and sodium-ion batteries use redox active transition-metal (TM) ions for charge compensation. For instance, upon charging $LiMn_2O_4$, Li^+ ions are removed with simultaneous oxidation of Mn^{3+} to Mn^{4+}.[1] In some cases, it is possible that additional Li^+ ions can be extracted upon charge at high voltages *via* oxygen-redox based reactions.[2–5] The use of both cation and anion redox couples offers an effective route to enhance the capacity of positive electrode materials and therefore, the energy density of batteries. However, most anion redox-active materials tend to exhibit large voltage hysteresis during the initial charge/discharge process, associated with cation migration from the transition-metal layers to the alkali metal layers which may lead to oxygen loss with simultaneous irreversible structural transformations that ultimately result in rapid capacity loss.[6–10] One sodium layered oxide which exhibits negligible voltage hysteresis and reversible oxygen anion redox is $Na_{4/7}[\square_{1/7}Mn_{6/7}]O_2$ (where $\square$ represents a transition metal vacancy).[11–15] The unique ordering between vacancies and manganese creates O 2*p* nonbonding orbitals which promotes oxygen redox activity. Upon cycling $Na_{4/7}[\square_{1/7}Mn_{6/7}]O_2$, the layered structure and ABBCCA oxygen stacking sequence is retained without migration of Mn cations. Therefore, $Na_{4/7}[\square_{1/7}Mn_{6/7}]O_2$ exhibits a low voltage hysteresis of 50 mV and enhanced anion redox reversibility compared with other sodium-based oxygen redox active materials.[13,15] However, when both cation and anion redox reactions are used, the capacity delivered by $Na_{4/7}[\square_{1/7}Mn_{6/7}]O_2$ fades by ~75 mA h g^{-1} over 60 cycles.[12,13] Partial substitution of Mn with Ti has proven to be an effective method to enhance the cycling performance of $Na_{4/7}[\square_{1/7}Mn_{6/7}]O_2$.[16,17] Liu *et al.* reported a superior capacity retention of 79% for $Na_{4/7}[\square_{1/7}Ti_{1/7}Mn_{5/7}]O_2$ compared with 17% for $Na_{4/7}[\square_{1/7}Mn_{6/7}]O_2$ between the voltage range 1.5–4.6 V at 50 mA g^{-1} over 60 cycles and a ultralow volume change of 0.11% upon initial charge/discharge.[16] In addition, Linnell *et al.* revealed no capacity loss for $Na_{4/7}[\square_{1/7}Ti_{1/7}Mn_{5/7}]O_2$ over the voltage range 3.0–4.4 V at 10 mA g^{-1} after 50 cycles, whilst $Na_{4/7}[\square_{1/7}Mn_{6/7}]O_2$ retained only 82% of its initial discharge capacity, arising from the low electronegativity of Ti that increases the Mn–O bond strength.[17] Moreover, $Na_{4/7}[\square_{1/7}Ti_{1/7}Mn_{5/7}]O_2$ operates at a higher potential owing to the low electronegativity of Ti which stabilizes the adjacent O 2*p* orbitals, as evidenced by DFT calculations.[17] These results demonstrate that Ti-substitution is an effective method to stabilize the structure, increase the charge/discharge voltage and enhance the cycling stability for $Na_{4/7}[\square_{1/7}Mn_{6/7}]O_2$.

[a] Dr. S. F. Linnell, Dr. E. Jeong Kim, Dr. A. B. Naden, Prof. J. T. S. Irvine, Dr. A. R. Armstrong
School of Chemistry
University of St Andrews
KY16 9ST St Andrews,
Fife, United Kingdom
E-mail: ara@st-andrews.ac.uk
[b] Dr. S. F. Linnell, Dr. E. Jeong Kim, Prof. J. T. S. Irvine, Dr. A. R. Armstrong
The Faraday Institution
Quad One, Harwell Science and Innovation Campus,
OX11 0RA Didcot, United Kingdom
[c] Dr. L. Anh Ma, Dr. R. Younesi
Department of Chemistry-Ångström Laboratory
Uppsala University
S-75121 Uppsala, Sweden
[d] Dr. L. C. Duda
Department of Physics and Astronomy,
Division of Molecular and Condensed Matter Physics
Uppsala University
S-75120 Uppsala, Sweden

Supporting information for this article is available on the WWW under https://doi.org/10.1002/celc.202200929

In contrast to honeycomb ordering, as observed for $Na_{4/7}[\square_{1/7}Mn_{6/7}]O_2$ and most other oxygen redox-active materials,[18–20] the ribbon superstructure is exhibited by P2-type $Na_{0.6}Li_{0.2}Mn_{0.8}O_2$, and the Mn/Li ordering in the transition-metal layers hinders Mn migration. As a result, P2-$Na_{0.6}Li_{0.2}Mn_{0.8}O_2$ presents a small voltage hysteresis of 0.2 V and shows that the ribbon ordering in $Na_{0.6}Li_{0.2}Mn_{0.8}O_2$ is essentially retained upon cycling.[18] The P3-type $Na_{0.67}Li_{0.2}Mn_{0.8}O_2$ material presents the same type of ribbon ordering in the transition metal layers as P2-$Na_{0.6}Li_{0.2}Mn_{0.8}O_2$ but with different oxygen stacking sequence, and similarly shows a small voltage hysteresis and highly reversible anion redox process.[10,21] More recently, Kim *et al.* explored the effects of Mn/Li ordering in the transition-metal layer on the electrochemical properties by preparing P3-$Na_{0.67}Li_{0.2}Mn_{0.8}O_2$ using different oxidizing atmospheres, dwell times and cooling rates. Kim *et al.* reported a narrow voltage hysteresis of 0.1 V for these materials and *in-situ* synchrotron PXRD revealed that the ribbon superstructure is retained upon charge/discharge with minimal changes in the unit cell volume (~0.15%), while Li^+ ions migrate reversibly between the transition-metal and Na layers.[22]

These materials demonstrate that ordering in the transition-metal layers can suppress cation migration and therefore deliver a small first cycle voltage hysteresis. Despite this, their cyclability and rate capability remain a key challenge, but doping strategies have proven to enhance the performance of anion redox active materials. Among the transition metal dopants investigated, substituting Mn with Ti has gained substantial attention owing to its low-cost, chemical stability, and widespread distribution.[16,17,23–25] Partial substitution of Mn by Ti in P2-type $Na_{0.72}Li_{0.24}Ti_{0.10}Mn_{0.66}O_2$ revealed remarkably improved oxygen anion redox reversibility with an exceptional reversible capacity of 165 mA h g^{-1} over 80 cycles and a capacity retention of 85%.[25] Recently it has been reported that Ti-substitution in P3-$Na_{0.6}Li_{0.2}Ti_{0.2}Mn_{0.6}O_2$ caused a drastic reduction in anion redox reversibility when a Ti-substitution level of 20% was used and the ribbon superstructure was lost on cycling and converted into a honeycomb-type ordering.[26] In this study we prepared a material with the lower Ti-substitution level of 15% ($Na_{0.67}Li_{0.2}Ti_{0.15}Mn_{0.65}O_2$) using a different synthetic method and annealed under oxygen. These changes resulted in a material with enhanced Mn/Li/Ti ordering in the transition metal layer compared with that reported in earlier work,[26] resulting in improved anion redox reversibility. Electrochemical testing revealed that when both cation (Mn^{3+}/Mn^{4+}) and anion (O^{2-}/O_2^{n-}) redox reactions are utilized, 15% Ti-substituted $Na_{0.65}Li_{0.2}Ti_{0.15}Mn_{0.65}O_2$ exhibits reversible anion redox and improved capacity retention of 89% after 30 cycles over the voltage range 1.6–4.4 V at 10 mA g^{-1} compared to $Na_{0.67}Li_{0.2}Mn_{0.8}O_2$ which shows 80% of its initial discharge capacity. The structural and electronic structural changes were investigated upon the initial charge/discharge which shows retention of the ribbon superstructure. This is in contrast with the observed behavior of the 20% Ti substituted material,[26] although the reversibility is less than that of $Na_{0.67}Li_{0.2}Mn_{0.8}O_2$.[27] Additionally, $Na_{0.67}Li_{0.2}Ti_{0.15}Mn_{0.65}O_2$ was cycled versus Li/Li^+ over the voltage range 2.0–4.8 V at 10 mA g^{-1} and shows an initial discharge capacity of 213.3 mA h g^{-1} is reached and 82% capacity retention after 30 cycles. This study on Ti-substituted P3-$Na_{0.67}Li_{0.2}Ti_{0.15}Mn_{0.65}O_2$ extends our understanding of oxygen-redox active P3-type sodium layered oxides,[22,28] and the significance of doping with Ti^{4+} and structural ordering on stabilizing the anion redox reversibility and cycling performance.[17]

Results and Discussion

Characterization of as-synthesized materials

$Na_{0.67}Li_{0.2}Mn_{0.8}O_2$ and $Na_{0.67}Li_{0.2}Ti_{0.15}Mn_{0.65}O_2$ were synthesized by a co-precipitation method and annealed under oxygen (referred to as Oxy-20Li and Oxy-20Li15Ti, respectively).[28] PXRD patterns of as-synthesized Oxy-$Na_{0.67}Li_{0.2}Mn_{0.8}O_2$ and Oxy-$Na_{0.67}Li_{0.2}Ti_{0.15}Mn_{0.65}O_2$ (Figure S1) were collected using Mo Kα_1 radiation ($\lambda = 0.70930$ Å) and the major diffraction peaks can be indexed to an ideal P3 structure with the space group *R*3 *m* in which Na^+ ions occupy trigonal prismatic sites and $Mn^{3+/4+}$, Li^+ and Ti^{4+} ions are in octahedral sites with ABBCCA oxygen stacking (Figure 1 (a) top image). However, numerous peaks are unindexed using this model (highlighted in Figure S1), instead all diffraction peaks can be fully indexed using a lower symmetry triclinic unit cell (space group $P\bar{1}$), consistent with previous work on P3-type $Na_xLi_{0.2}Mn_{0.8}O_2$ ($0.6 \leq x \leq 0.67$).[18,27] Therefore, a Rietveld refinement was performed using the same ribbon superstructure. model ($a_{super} \approx \sqrt{7}a$, $b_{super} \approx \sqrt{3}a$) as that used for P3-$Na_{0.67}Li_{0.2}Mn_{0.8}O_2$, where the Li^+ ions separate ribbons composed of four Mn ions.[27] In the case of Oxy-$Na_{0.67}Li_{0.2}Ti_{0.15}Mn_{0.65}O_2$, it was apparent that the degree of ordering in the transition metal layer was lower than that seen in P3-$Na_{0.67}Li_{0.2}Mn_{0.8}O_2$. This is not unexpected since the ionic radius of Ti^{4+} (0.605 Å) lies between those of Li^+ (0.76 Å) and Mn^{4+} (0.53 Å),[29] leading to a smaller driving force for superlattice formation. In the final refinement it was assumed that any disorder of transition-metal ions on to the lithium site exclusively involved Ti^{4+} ions, with Mn, Ti and Li distributed over the transition metal sites with values corresponding to the overall stoichiometry (Figure 1 (a) bottom image). The obtained profile fit, and corresponding structural parameters are given in Figure 1 (b) and Table S1, respectively. The morphology of Oxy-$Na_{0.67}Li_{0.2}Ti_{0.15}Mn_{0.65}O_2$ was examined by SEM and a micrograph representative of the sample is shown in Figure 1 (c). This shows a uniform distribution of agglomerated particles of roughly 100 nm in size. EDS elemental maps (excluding Li) are given in Figure 1 (d) and show even elemental distribution of sodium, manganese, and oxygen but shows regions which are slightly rich in titanium. However, there is no evidence of any titanium-containing impurity from the PXRD data (Figure 1 (b)).

Electrochemical properties

Initial investigation of the electrochemical properties of Oxy-$Na_{0.67}Li_{0.2}Ti_{0.15}Mn_{0.65}O_2$ was carried out in sodium-half cells at

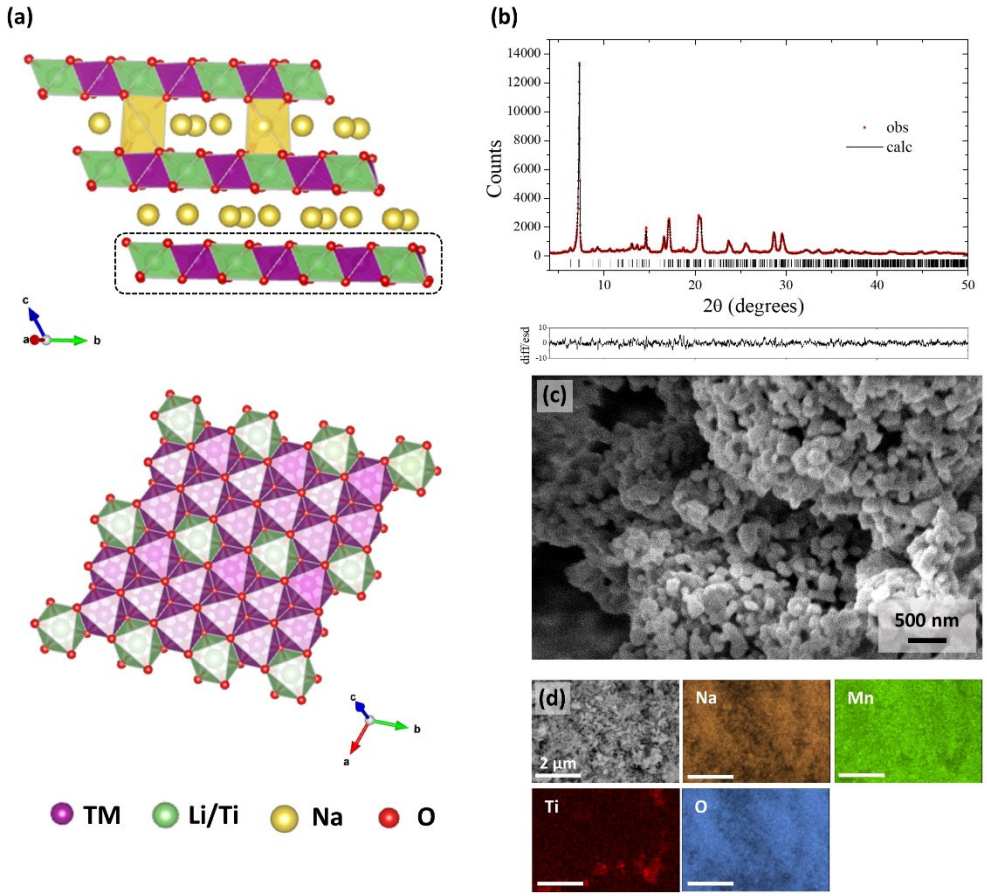

Figure 1. (a) Crystal structure of Oxy-$Na_{0.67}Li_{0.2}Ti_{0.15}Mn_{0.65}O_2$. The top image shows the alternating layers of Na^+ ions and TMO_2 slabs. The bottom image shows the superlattice structure. (b) Laboratory X-ray Rietveld refinement of as-synthesized Oxy-$Na_{0.67}Li_{0.2}Ti_{0.15}Mn_{0.65}O_2$. Observed data points are shown in red, with fitted profile in black and tick marks indicate the allowed reflections for the $P\bar{1}$ phase. (c) SEM micrograph of as-synthesized Oxy-$Na_{0.67}Li_{0.2}Ti_{0.15}Mn_{0.65}O_2$, and (d) EDS mapping of the elements of Na, Mn, Ti, and O.

30 °C using 1 M $NaClO_4$ in propylene carbonate containing 3% fluoroethylene carbonate by weight as electrolyte. Oxy-$Na_{0.67}Li_{0.2}Ti_{0.15}Mn_{0.65}O_2$ was cycled galvanostatically within the voltage range 1.8–4.4 V at 10 mA g^{-1} and the performance is shown in Figure 2(a). Oxy-$Na_{0.67}Li_{0.2}Ti_{0.15}Mn_{0.65}O_2$ delivers an initial discharge capacity of 178 mA h g^{-1} and shows satisfactory capacity retention. The charge/discharge profiles (Figure 2(b)) for the second cycle show a plateau on charge, which is partially reversible upon discharge. The reversible redox process observed over the high voltage region (beyond 4.0 V) for Li-substituted sodium manganese oxides, $Na_xLi_yMn_{1-y}O_2$, adopting either P2 or P3 structures has been ascribed to anion redox originating from oxygen anions in Li–O–Na local configurations, as determined by structural and spectroscopic studies.[18,21,30] As shown in Figure 2(b) the oxygen anion redox activity for Oxy-$Na_{0.67}Li_{0.2}Ti_{0.15}Mn_{0.65}O_2$ persists over several cycles but progressively decays and is no longer observed after 25 cycles. This is accompanied by a systematic increase in the voltage associated with the $Mn^{3+/4+}$ redox couple (Figure 2(c)) which is consistent with similar sodium manganese-based layered oxides.[27]

In the region beyond which the anion redox is lost, the average potential for the $Mn^{3+/4+}$ redox couple increases from 2.68 V to 2.72 V between cycles 20 and 40. The anion redox stability is in contrast with that reported for the higher Ti substitution level of 20% which shows an essentially irreversible oxygen anion redox process thus demonstrating the importance both of Ti content and synthetic method in dictating anion redox reversibility.[26]

In addition, cyclic voltammograms were collected between 1.8–4.4 V at a scan rate of 15 µV s^{-1}, as shown in Figure 2(d). These data similarly show a reversible redox process centered about 4.10 V associated with oxygen anion redox and an increasing oxidation voltage associated with $Mn^{3+/4+}$ upon cycling, consistent with the galvanostatic cycling data (Figure 2(c)).[31,32]

In order to evaluate the effect of Ti^{4+}-substitution on the electrochemical performance, further studies were performed on sodium-half cells of Oxy-$Na_{0.67}Li_{0.2}Mn_{0.8}O_2$ and Oxy-$Na_{0.67}Li_{0.2}Ti_{0.15}Mn_{0.65}O_2$ were cycled in the wider voltage range 1.6–4.4 V at 10 mA g^{-1} at 30 °C. The galvanostatic cycling performances are compared in Figure 3(a) which demonstrates that both materials deliver comparable discharge capacities over the first ten cycles. On subsequent cycles, the discharge capacity of Oxy-$Na_{0.67}Li_{0.2}Mn_{0.8}O_2$ decreases more rapidly, retaining only 65% of its initial discharge capacity (179.8 mA h g^{-1}) after 50 cycles. In comparison, Oxy-$Na_{0.67}Li_{0.2}Ti_{0.15}Mn_{0.65}O_2$ main-

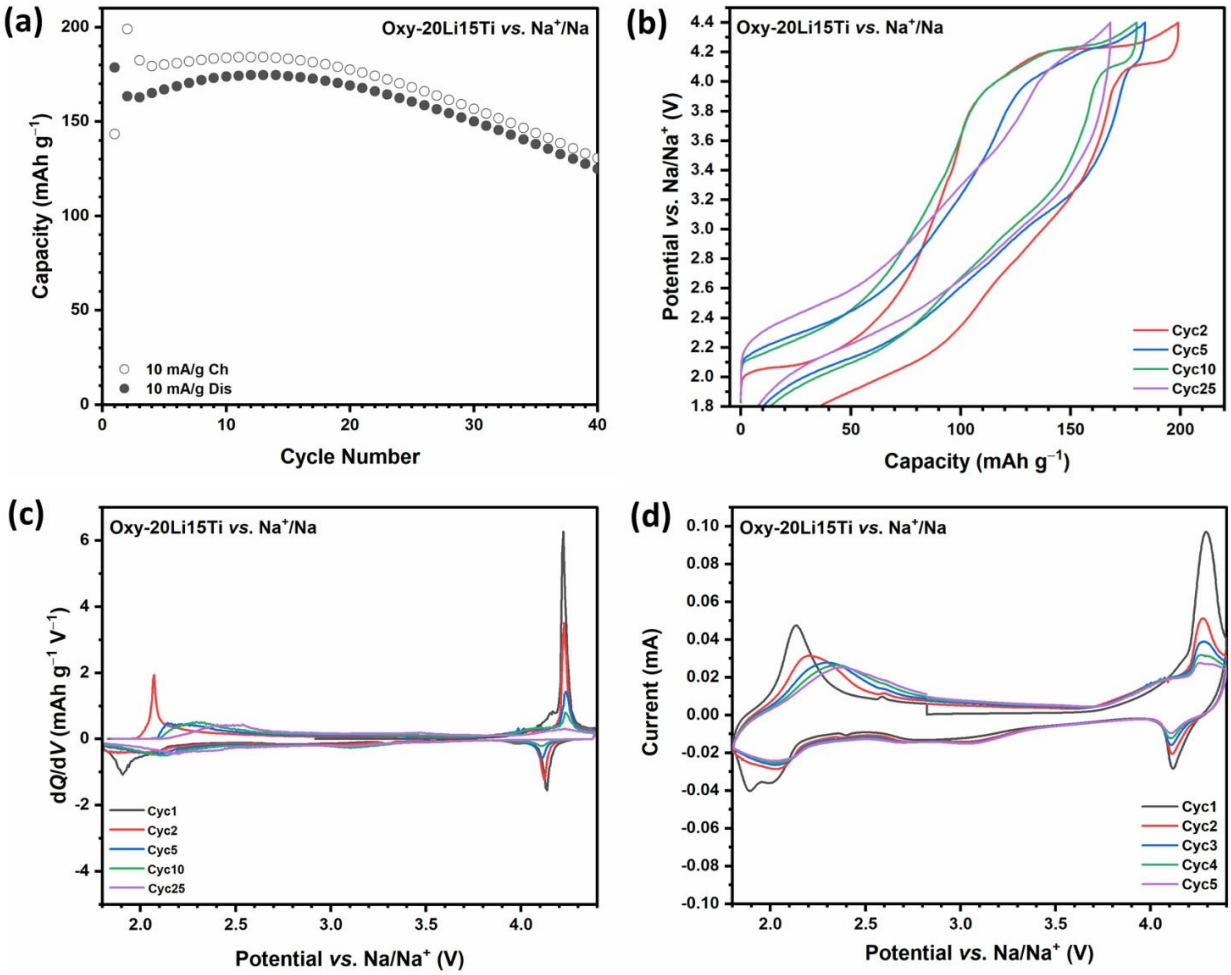

Figure 2. (a) Galvanostatic cycling performance Oxy-20Li15Ti cycled versus Na/Na^+ at 30 °C in the voltage range 1.8–4.4 V at a current rate of 10 mA g^{-1} using 1 M $NaClO_4$ in propylene carbonate containing 3% fluoroethylene carbonate by weight as electrolyte. Empty and filled circles represent charge and discharge capacities, respectively. (b) Charge/discharge profiles and (c) the corresponding differential capacity versus voltage plot of Oxy-20Li15Ti, showing the second (red), fifth (blue), tenth (green) and twenty-fifth (purple) cycles. (d) Voltammetric analysis for Oxy-20Li15Ti collected at a scan rate of 15 μV s^{-1}.

tains 75% of its initial discharge capacity (187.9 mA h g^{-1}) after 50 cycles, thereby demonstrating the stabilizing role of Ti^{4+}-substitution on the cycling performance, consistent with other Ti^{4+}-substituted systems.[16,17,23–25] Cao *et al.*[31] reported enhanced performance in P2-$Na_{0.66}Li_{0.22}Ti_{0.15}Mn_{0.63}O_2$ with a honeycomb ordering and assigned this to a reduction in Jahn-Teller distortion on cycling whilst Li *et al.*[25] also reported the effects of Ti^{4+}-substitution in P2-$Na_xLi_yMn_{1-y}O_2$. They used EPR to suggest that anisotropic coupling between Mn^{4+} and O_2^{n-} in the Li doped material is reduced by co-doping thereby enhancing reversibility. Zhao et al.[32] reported that Ti^{4+}-substitution in P2-$Na_{2/3}Mg_{1/3}Ti_{1/6}Mn_{1/2}O_2$ enhances reversibility by decreasing ordering which enhances structural stability. While Oxy-$Na_{0.67}Li_{0.2}Ti_{0.15}Mn_{0.65}O_2$ presents greater overall cycling stability, the charge/discharge profiles for the second cycle (Figure 3(b)) reveal more reversible oxygen anion redox behavior for Oxy-$Na_{0.67}Li_{0.2}Mn_{0.8}O_2$ which also shows a smaller voltage hysteresis of 140 mV (Figure 3(d)) compared to Oxy-$Na_{0.67}Li_{0.2}Ti_{0.15}Mn_{0.65}O_2$ which reveals a voltage hysteresis of 180 mV. Previous work has demonstrated that cation ordering in the transition metal layers influences the capability of a material to stabilize the oxidized oxygen species.[18] Ribbon-type ordered materials have been shown to prevent in-plane Mn migration and therefore the formation of trapped molecular O_2. The usually large voltage hysteresis observed for oxygen redox active materials is suppressed because of the stable coordination environment surrounding the oxygen anions in the ribbon-type structure.[18] In the case of Oxy-$Na_{0.67}Li_{0.2}Mn_{0.8}O_2$, the smaller voltage hysteresis (0.15 V) may be associated with the high degree of Li-Mn ordering. As for Oxy-$Na_{0.67}Li_{0.2}Ti_{0.15}Mn_{0.65}O_2$, which also exhibits a ribbon superlattice structure, when Ti^{4+} (0.605 Å) ions are introduced, their intermediate size compared with Mn^{4+} (0.53 Å) and Li^+ (0.76 Å) ions creates disorder in the ribbon superlattice, resulting in a slightly greater voltage hysteresis of 0.18 V (Figure 3(b)). However analogous to Oxy-$Na_{0.67}Li_{0.2}Ti_{0.15}Mn_{0.65}O_2$, Figure 3(d) shows that the oxygen redox activity of Oxy-$Na_{0.67}Li_{0.2}Mn_{0.8}O_2$ deteriorates and is no longer

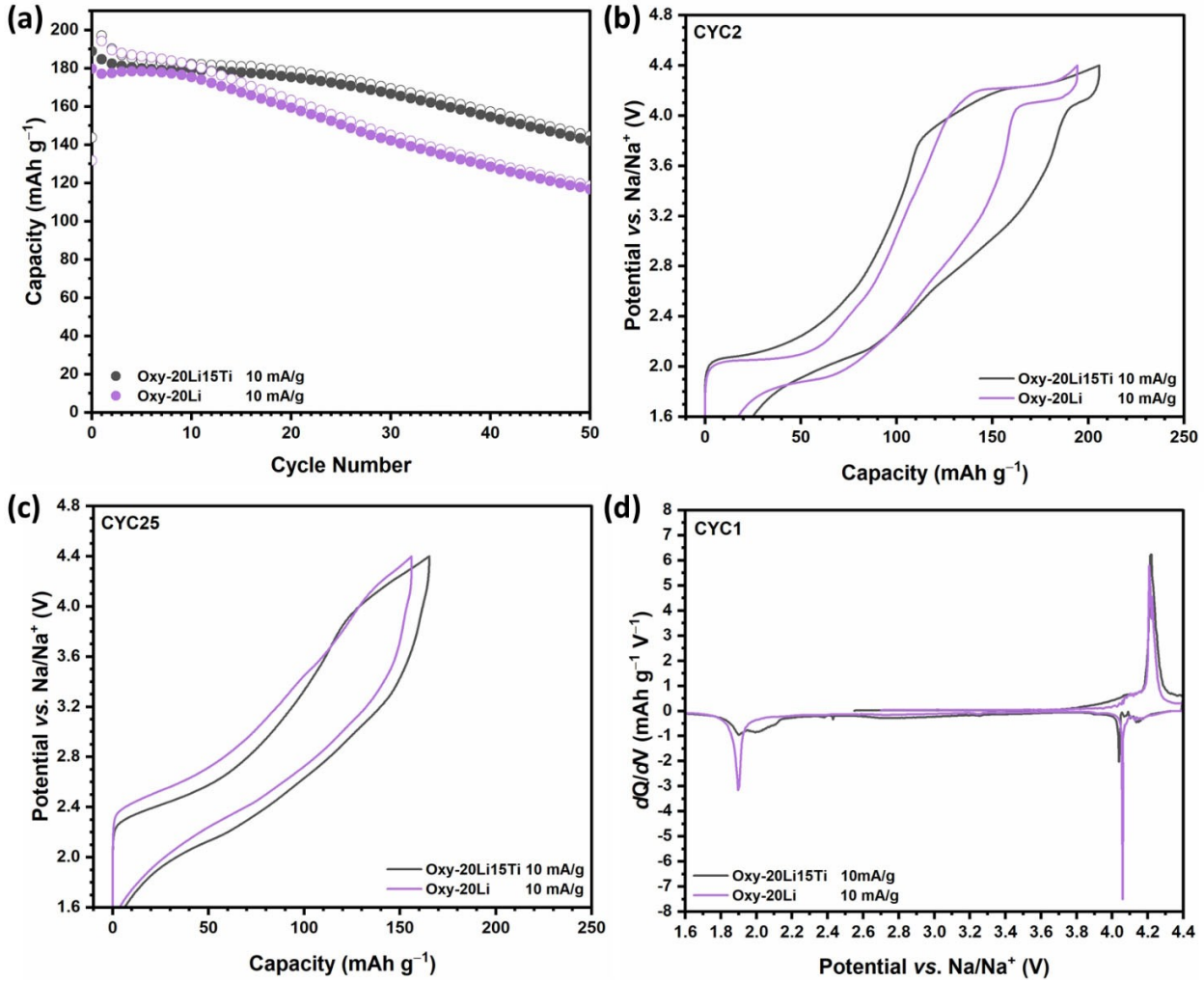

Figure 3. (a) Galvanostatic cycling performance of Oxy-20Li15Ti (black) and Oxy-20Li (purple) cycled versus Na/Na^+ in the voltage range 1.6–4.4 V at 10 mA g^{-1} at 30 °C, using 1 M $NaPF_6$ in ethylene carbonate/diethyl carbonate (1 : 1 v/v %) as the electrolyte. Empty and filled circles represent charge and discharge capacities, respectively. (b) Charge/discharge profiles for the second cycle and (c) twenty-fifth cycle, and (d) differential capacity versus voltage plot showing the first cycle for Oxy-20Li15Ti (black) and Oxy-20Li (purple) cycled in the voltage range 1.6–4.4 V at 10 mA g^{-1} at 30 °C.

evident after 25 cycles at 10 mA g^{-1}, consistent with the observed capacity fade (Figure 3 (a)).

The cycling performance of Oxy-$Na_{0.67}Li_{0.2}Ti_{0.15}Mn_{0.65}O_2$ was also investigated at a variety of charge-discharge rates 10, 200 and 500 mA g^{-1} in the voltage range 1.6–4.4 V, using $NaClO_4$ in propylene carbonate containing 3 % fluoroethylene carbonate by weight as electrolyte. These data are presented in Figure 4. Figure 4 (a) shows that Oxy-$Na_{0.67}Li_{0.2}Ti_{0.15}Mn_{0.65}O_2$ delivers an initial discharge capacity of 190.8 mA h g^{-1} at 10 mA g^{-1} and shows a significant fade in capacity after 20 cycles. Whereas at the fast rates the capacity decreases over the first few cycles and then stabilizes. Increasing the rate by a factor of 20 results in a loss in initial capacity of roughly 10 % and shows a capacity loss of only 28 % after 50 cycles. Increasing the rate further to 500 mA g^{-1}, results in a capacity fade of 45 % after 50 cycles. Figure 4 (b) shows the charge/discharge profiles of the second cycle at 10, 200 and 500 mA g^{-1}, demonstrating that at the faster rates the high voltage redox process, associated with oxygen anion redox, is more reversible than at the slower rate of 10 mA g^{-1}. This is confirmed from Figure 4 (c) which shows that the oxygen anion redox process persists even after 25 cycles at the faster rates (200 and 500 mA g^{-1}). By contrast, at 10 mA g^{-1} the oxygen anion redox process is no longer evident, consistent with the rapid capacity fade observed after 20 cycles (Figure 4 (a)). This can be attributed to reduced reaction with the electrolyte at the faster rates, resulting in enhanced reversibility. While the initial capacity loss observed at the faster rates is probably due to the increase in polarization as shown in Figure 4 (d). These results are consistent with those previously observed for Oxy-$Na_{0.67}Li_{0.2}Mn_{0.8}O_2$.[27]

The electrochemical properties of Oxy-$Na_{0.67}Li_{0.2}Ti_{0.15}Mn_{0.65}O_2$ was also investigated in lithium-half cells at 30 °C. Oxy-$Na_{0.67}Li_{0.2}Ti_{0.15}Mn_{0.65}O_2$ was cycled galvanostatically within the voltage range of 2.0–4.8 V at 10 and 50 mA g^{-1}. The resulting cycling performance is shown in Figure 5 (a). At a rate of 10 mA g^{-1} an initial discharge capacity of 213.3 mA h g^{-1} is

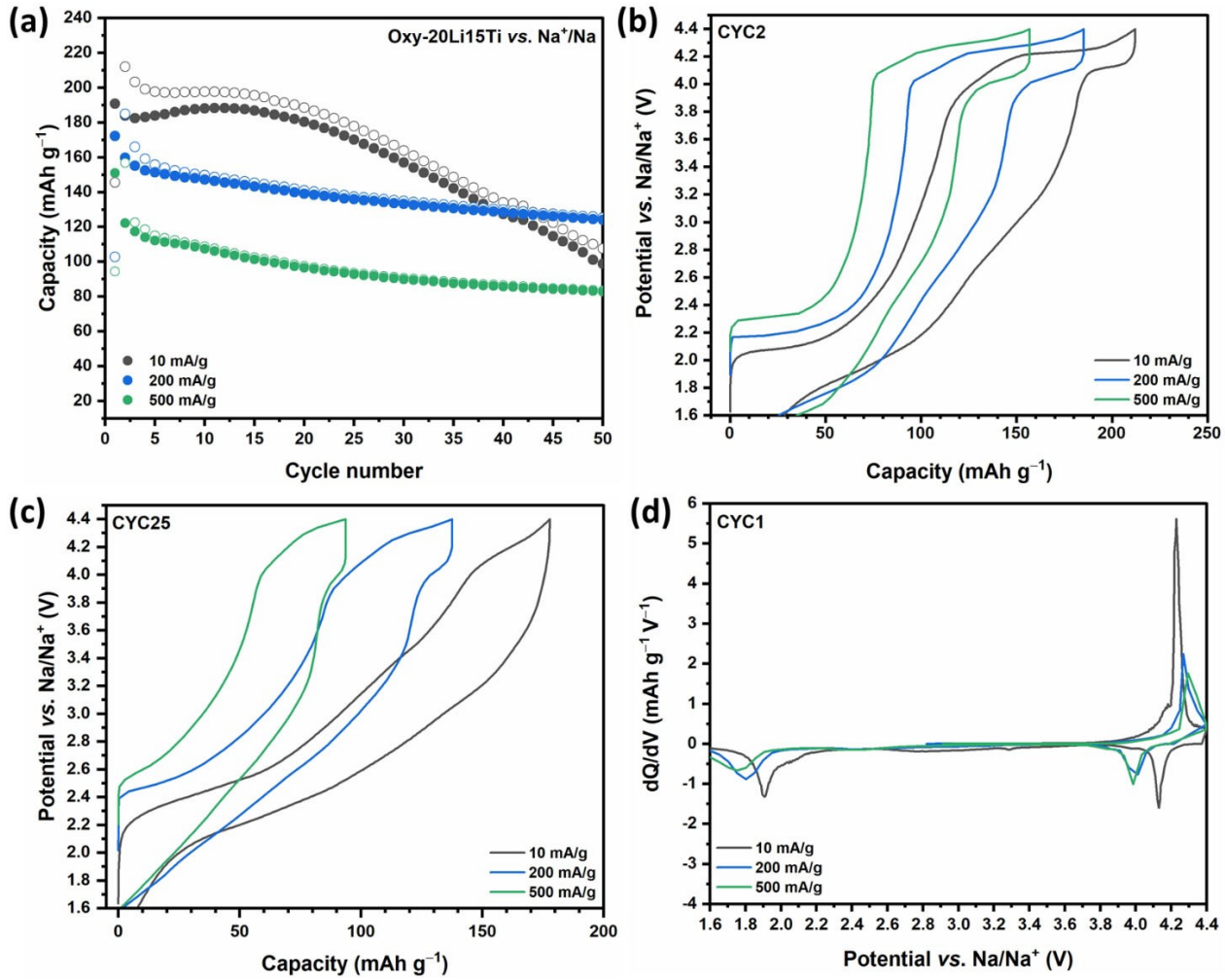

Figure 4. (a) Galvanostatic cycling performance of Oxy-20Li15Ti cycled versus Na/Na^+ in the voltage range 1.6–4.4 V at 10 (black), 200 (blue) and 500 mA g^{-1} (green) at 30 °C, using 1 M $NaClO_4$ in propylene carbonate containing 3% fluoroethylene carbonate by weight as electrolyte. Empty and filled circles represent charge and discharge capacities, respectively. (b) Charge/discharge profiles for the second cycle and (c) twenty-fifth cycle, and (d) differential capacity versus voltage plot for the first cycle for Oxy-20Li15Ti cycled in the voltage range 1.6–4.4 V at 10 (black), 200 (blue) and 500 mA g^{-1} (green) at 30 °C, using 1 M $NaClO_4$ in propylene carbonate containing 3% fluoroethylene carbonate by weight as electrolyte.

reached and the capacity fades more rapidly after the first 10 cycles, maintaining of 75% its initial capacity after 50 cycles. Increasing the current rate to 50 mA g^{-1} resulted in a loss of discharge capacity of approximately 7% initially but exhibits an improved capacity retention of 81% after 50 cycles. Figure 5(a) further shows that at the faster rate the capacity drops over the first few cycles and then stabilizes thereafter, demonstrating that there are fewer side-reactions at the faster rate. The charge/discharge profiles for the first cycle are shown in Figure 5(b), revealing a different profile from those observed when Oxy-$Na_{0.67}Li_{0.2}Mn_{0.8}O_2$ is cycled versus Na/Na^+. Figure 5(b) shows an extended irreversible plateau on charging at approximately 4.5 V, with a sloping plateau at roughly 3.0 V, associated with the reduction of Mn^{4+} to Mn^{3+} as Li^+ ions are inserted upon discharge. The corresponding d*Q*/d*V* plot for the first cycle shown in Figure 5(c). This is consistent with $Li_xMn_{1-y}Li_yO_2$ materials which similarly show a significant irreversible capacity at 4.5 V on the initial charge.[33,34] In $Li_xMn_{1-y}Li_yO_2$, $(0 \leq y \leq 0.2)$ Li^+ ion extraction occurs initially (below 4.0 V) *via* the oxidation of residual Mn^{3+} to Mn^{4+}. Subsequently, further Li^+ ions are extracted at 4.5 V, resulting in the oxidation of O^{2-} which leads to oxygen evolution and therefore the removal of Li_2O.[33–36] Therefore, when Oxy-$Na_{0.67}Li_{0.2}Ti_{0.15}Mn_{0.65}O_2$ is charged versus Li/Li^+, the irreversible plateau observed at 4.5 V on the initial charge can be reasonably attributed to oxidation of O^{2-} and the effective removal of Na_2O and Li_2O. It is also recognized that on charging to the high voltages (beyond 4.5 V) the electrolyte decomposes forming H^+ ions which exchanges for Li^+ ions in the electrode.[33] Upon subsequent cycling, Figure 5(d) shows only a reversible plateau at approximately 3.0 V associated with the $Mn^{3+/4+}$ redox couple. Figure S2(a) and (b) show the charge/discharge profiles for Oxy-$Na_{0.67}Li_{0.2}Ti_{0.15}Mn_{0.65}O_2$ versus Li/Li^+ cycled between 2.0–4.8 V at 50 mA g^{-1} and the corresponding d*Q*/d*V* plots, respectively. After 50 cycles, Figure S2(b) shows a double peak at roughly 4.0 V, indicative of the formation of a spinel-like structure, consistent with previous

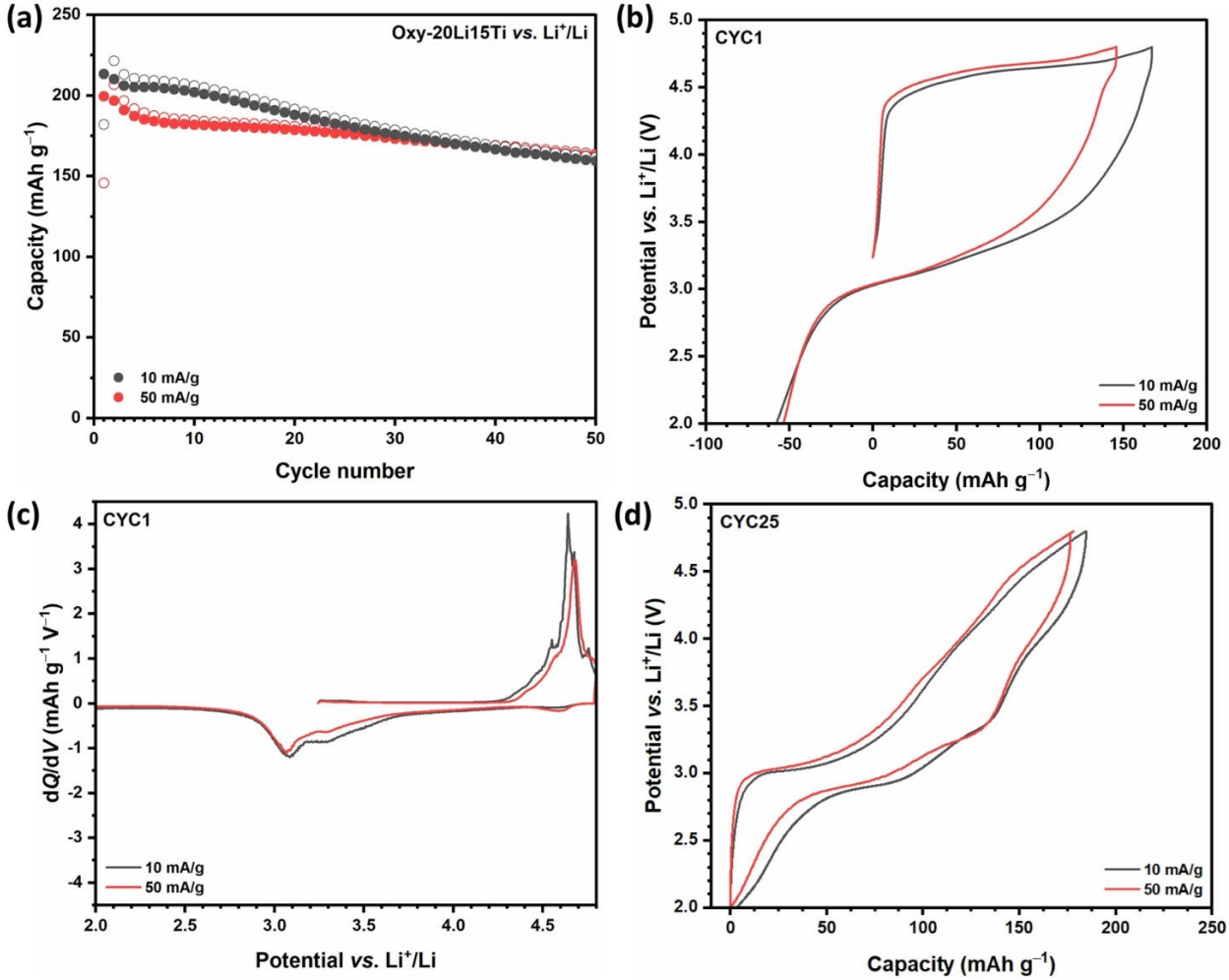

Figure 5. (a) Galvanostatic cycling performance of Oxy-20Li15Ti cycled versus Li/Li^+ in the voltage range 2.0–4.8 V at 10 (black) and 50 mA g^{-1} (red) at 30 °C, using 1.0 M $LiPF_6$ ethylene carbonate/dimethyl carbonate (50/50 v/v) as electrolyte. Empty and filled circles represent charge and discharge capacities, respectively. (b) Charge/discharge profiles for the first cycle and (d) twenty-fifth cycle, and (c) differential capacity versus voltage plot for the first cycle for Oxy-20Li15Ti cycled in the voltage range 2.0–4.8 V at 10 (black) and 50 mA g^{-1} (red) at 30 °C, using 1.0 M $LiPF_6$ ethylene carbonate/dimethyl carbonate (50/50 v/v) as electrolyte.

reports on $LiMnO_2$ and $Li_xMn_{1-y}Li_yO_2$ materials.[33,37,38] Figure S2 (b) also reveals a reversible response centered at about 3.0 V which is consistent with Li in octahedral sites, the presence of a process on discharge at 3.5 V which gradually shifts to lower potentials upon cycling is indicative of the progress of the transformation to the spinel-type structure. This structural transformation involves the migration of roughly 25% Mn ions from the octahedral sites in the transition-metal layers into octahedral sites in the Li layers, and the displacement of Li^+ ions in the Li layers to tetrahedral sites.[37,38]

Structural evolution

Powder X-ray diffraction patterns for Oxy-$Na_{0.67}Li_{0.2}Mn_{0.8}O_2$ were collected *ex-situ* at various states of charge and discharge on the first cycle within the voltage range 1.8–4.4 V at 10 mA g^{-1} to establish the structural changes The evolution of the PXRD patterns is presented in Figure 6 (a) which demonstrates a solid-solution behavior for Oxy-$Na_{0.67}Li_{0.2}Ti_{0.15}Mn_{0.65}O_2$, with no additional phases forming, apart from the appearance of two minor peaks at 5.77 and 11.58° after charge to 4.4 V. These peaks correspond to a hydrated oxide phase, due to the incorporation of water molecules into the sodium layers of sodium-deficient layered oxides. Hydrate phases commonly form in highly charged states of sodium-deficient layered oxides and only a minor amount is observed here.[39–41] Rietveld refinements were performed, and the fits obtained for data from the electrodes charged to 4.1 and 4.4 V and after subsequent discharge to 1.8 V are shown in Figure 6 (b–d), respectively. These data show that upon Na^+ ion extraction and insertion the superlattice structure is retained (as highlighted in Figure 6 (a)) and good fits were reached using the ribbon superlattice model with the space group $P\bar{1}$. This trend agrees with *in-situ* synchrotron PXRD data for P3-type $Na_{0.67}Li_{0.2}Mn_{0.8}O_2$ annealed in air.[27] Whilst $Na_{0.67}Li_{0.2}Mn_{0.8}O_2$ reveals minimal volume changes (~0.15%), these data demonstrate that 15% Ti^{4+} substitution in the TMO_2 layer effectively leads to a negligible change in volume. This

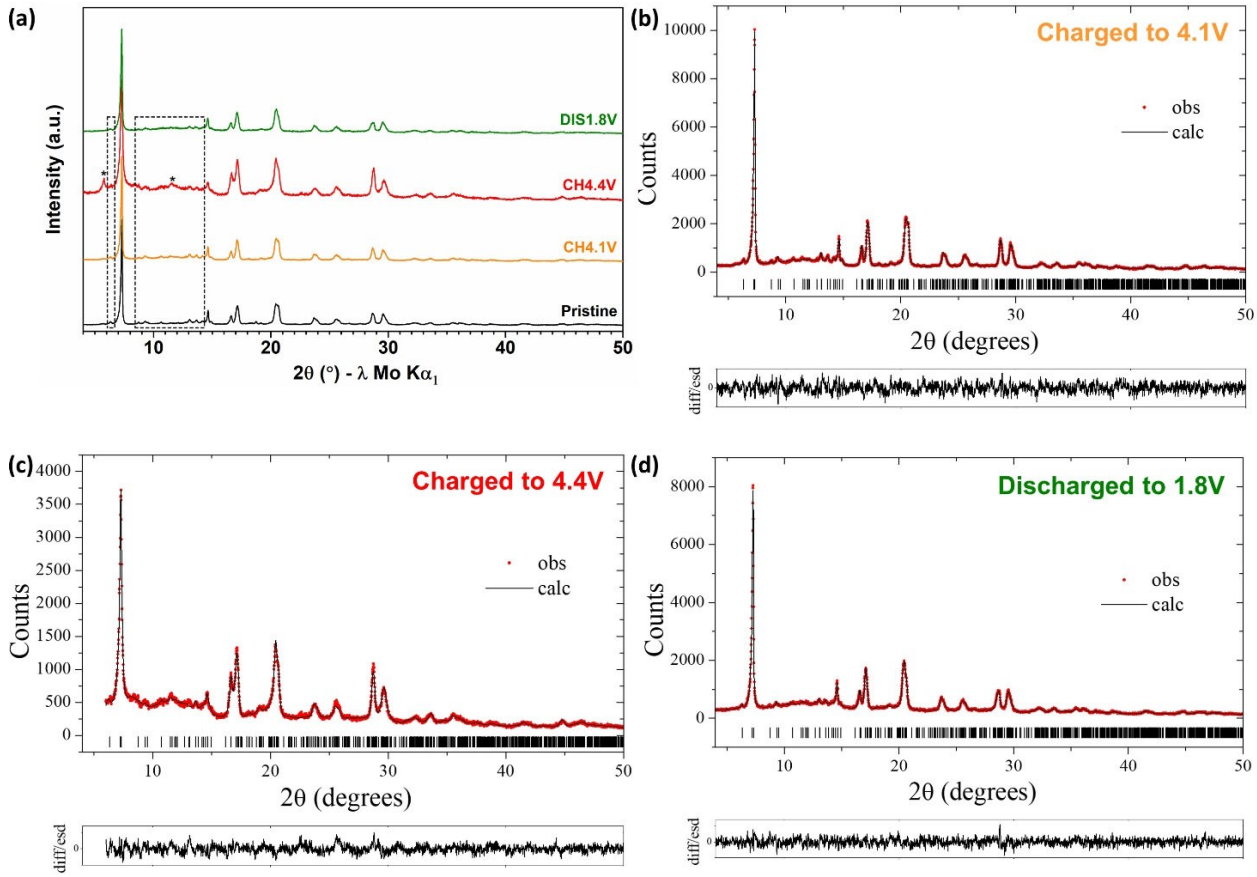

Figure 6. (a) Laboratory ex-situ PXRD data for as-prepared Oxy-$Na_{0.67}Li_{0.2}Ti_{0.15}Mn_{0.65}O_2$ (black), after charge to 4.1 V (orange), at the end of charge to 4.4 V (red), and after subsequent discharge to 1.8 V (green). The superstructure peaks are located in the dotted regions of the diffraction patterns. Symbol (*) indicates hydrate diffraction peaks. Rietveld fits of Oxy-$Na_{0.67}Li_{0.2}Ti_{0.15}Mn_{0.65}O_2$ (b) after charge to 4.1 V, (c) after charge to 4.4 V, and (d) after subsequent discharge to 1.8 V. Observed data points are shown in red with fitted profiles in black. Tick marks indicate allowed reflections.

suggests enhanced structural stability which may provide the origin for the improved cyclability of $Na_{0.67}Li_{0.2}Ti_{0.15}Mn_{0.65}O_2$ relative to $Na_{0.67}Li_{0.2}Mn_{0.8}O_2$ as shown in Figure 3(a). It is also interesting to note that this finding differs from a recent study on P3-$Na_{0.6}Li_{0.2}Ti_{0.2}Mn_{0.6}O_2$ which found that the ribbon superstructure is converted to honeycomb-type ordering as a result of substantial TM migration which also accounts for the irreversibility of the anion redox process.[26] This shows the importance of both dopant concentration and also synthetic method in controlling the reversibility of anion redox properties of ostensibly highly similar materials. The progressive increase in Ti concentration clearly reduces anion redox stability.

Electronic structural evolution

To investigate the charge compensation mechanism of Oxy-$Na_{0.67}Li_{0.2}Ti_{0.15}Mn_{0.65}O_2$, SXAS data at the Mn L-edge and O K-edge and RIXS O K-edge spectra were collected at different states of charge/discharge over the first cycle between the voltage range 1.8–4.4 V. SXAS spectra for the Mn L-edge were measured in the inverse partial fluorescence yield (IPFY) to give spectra representative of the bulk sample.[42] These data are presented in Figure 7(a) and (b), and compared to the spectra of Mn_2O_3 and MnO_2 reference compounds with manganese formal oxidation states of +3 and +4, respectively. The spectrum of pristine Oxy-$Na_{0.67}Li_{0.2}Ti_{0.15}Mn_{0.65}O_2$ presents a predominantly Mn^{4+} signature with absorption peaks at 641.1 and 643.7 eV, but also shows a small peak at 642.0 eV characteristic of Mn^{3+}. After charge to 4.1 V (Figure 7(a)), the feature at 642.0 eV intensifies and a shoulder appears at roughly 640 eV, which are both characteristic of Mn^{3+}. The shoulder at roughly 640 eV persists upon further charge to 4.22 and 4.4 V, whilst the intensity of the peak at 642.0 eV diminishes. At the end of discharge to 1.8 V, the spectrum reveals the features at both 640 and 642.0 eV, indicating the partial reduction of Mn^{4+} to Mn^{3+}. This trend is consistent with previous Mn L-edge data reported for Oxy-$Na_{0.67}Li_{0.2}Ti_{0.15}Mn_{0.65}O_2$.[27]

SXAS spectra of the O K-edge in the bulk sensitive partial fluorescence yield (PFY) mode for Oxy-$Na_{0.67}Li_{0.2}Ti_{0.15}Mn_{0.65}O_2$ at the same states of charge and discharge as were studied for the Mn K-edge spectra were collected. These data are presented in Figure 8(a) which show two absorption peaks below 533 eV. Changes in the integral of these peaks between 527 and 533 eV are given in Figure 8(b), relative to the pristine material and relate to changes in the density of empty states just above the

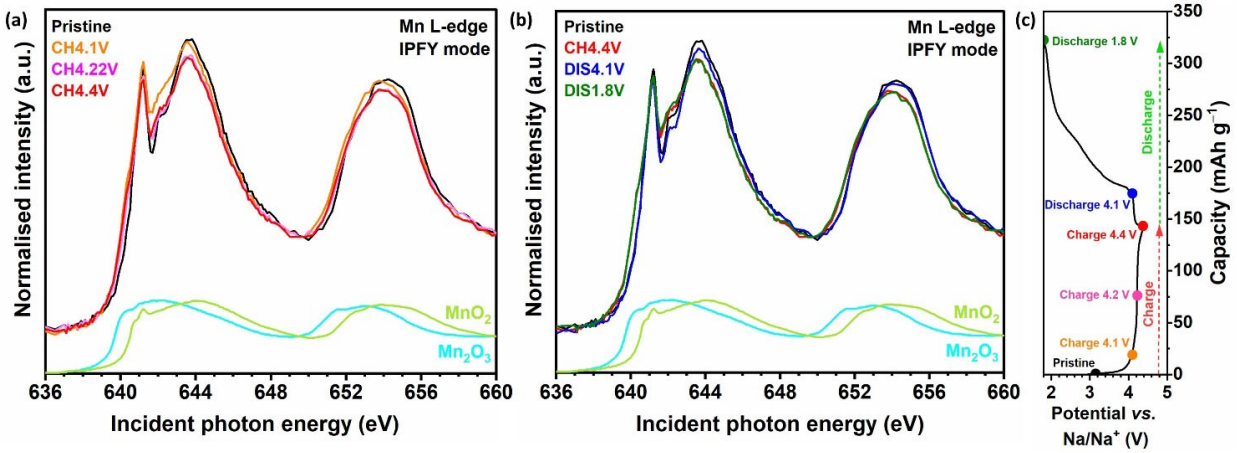

Figure 7. Normalized Mn L-edge SXAS spectra at various states of charge and discharge, collected in IPFY mode for Oxy-$Na_{0.67}Li_{0.2}Ti_{0.15}Mn_{0.65}O_2$, (a) as prepared (black), charge to 4.1 V (orange), 4.2 V (pink), 4.4 V (red), (b) as-prepared (black), charge to 4.4 V (red) and subsequent discharge to 4.1 V (blue) and 1.8 V (green). (c) The corresponding galvanostatic charge/discharge profile with the voltages highlighted where the ex-situ SXAS measurements were conducted.

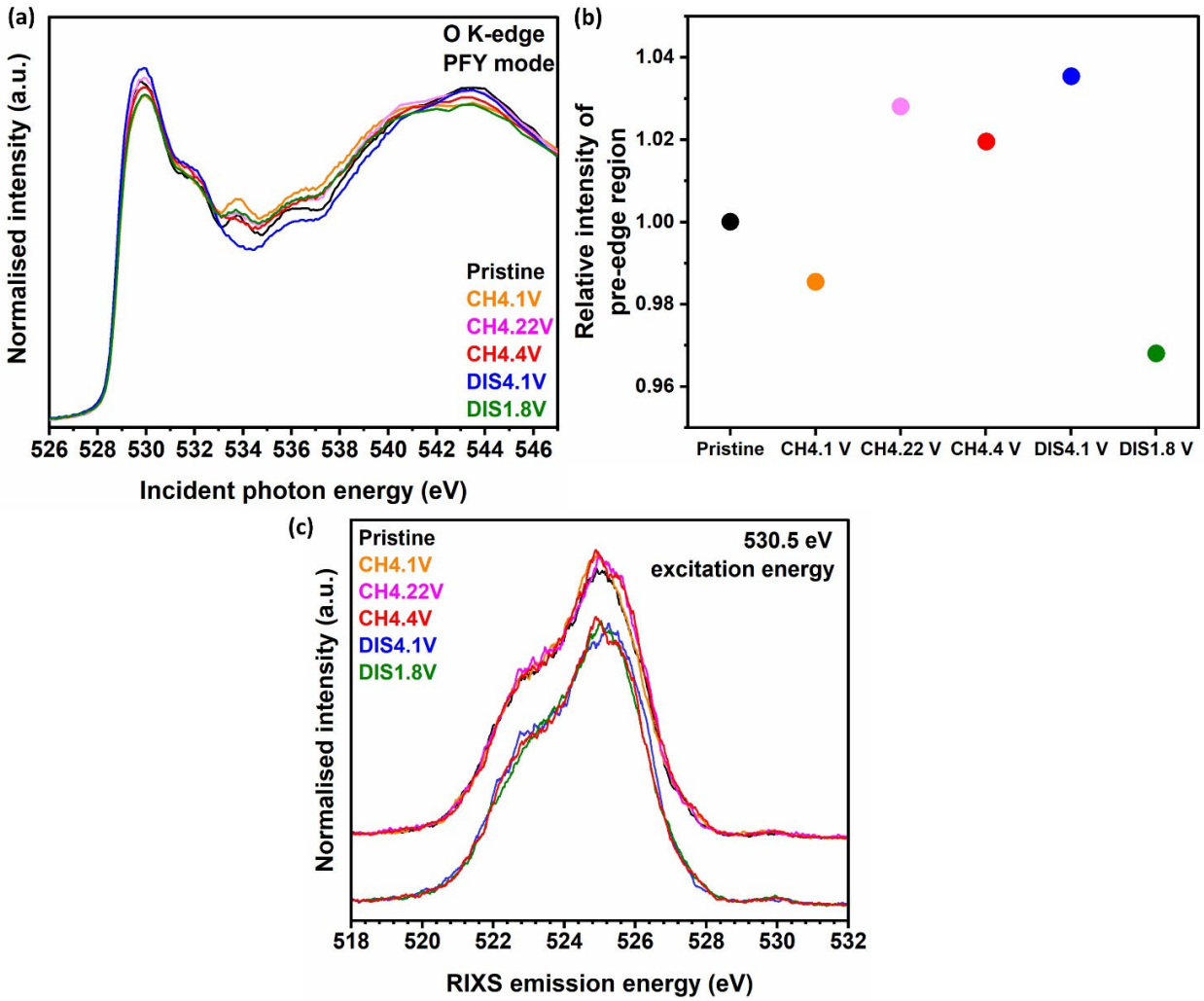

Figure 8. (a) Normalized O K-edge SXAS spectra at various states of charge and discharge, collected in PFY mode for Oxy-$Na_{0.67}Li_{0.2}Ti_{0.15}Mn_{0.65}O_2$. (b) The integrated intensity of the pre-edge feature (527.6–533.0 eV) for the O K-edge SXAS, relative to the pristine phase. (c) O K-edge RIXS spectra collected at an excitation energy of 530.5 eV for Oxy-$Na_{0.67}Li_{0.2}Ti_{0.15}Mn_{0.65}O_2$.

Fermi level which are influenced by the oxidation state of Mn and the covalency of the O 2*p* band.[43] Figure 8(b) reveals variations in the intensity which are consistent with changes observed in the Mn L-edge spectra (Figure 7) and can be attributed to hybridization between the O 2*p* states and TM 3*d* states.[22,27,44] After charge to 4.1 V, Figure 8(b) shows a decrease in intensity which is consistent with the appearance of Mn^{3+} features (Figure 7(a)). Upon further charge to 4.22 and 4.4 V and subsequent discharge to 4.1 V, the intensity fluctuates but is raised with respect to the pristine phase, demonstrating the removal of electrons from O 2*p* states

After discharge to 4.1 V, Figure 8(b) reveals a maximum which is likely connected to the disappearance of the peak at 534 eV as shown in Figure 8(a). On discharge to 1.8 V, the intensity decreases, indicative of the repopulation of the electron-holes of the O 2*p* states and is also consistent with the reduction to Mn^{3+}.

Oxygen K-edge RIXS spectra have been collected to investigate the electronic structural changes of the occupied O bands. Figure 8(c) shows the O K-edge RIXS spectra extending between ~521–528 eV for an excitation energy of 530.5 eV. Initially, the spectrum for the pristine material spectra peaks at an energy of about 525.4 eV. Charging then leads to the development of extra spectral intensity in adjacent energy regions. Upon discharge to 4.1 V further spectral restructuring is observed before eventually reverting to the shape observed for the pristine material again at 1.8 V. This evolution shows that whilst oxygen states participate during the charge/discharge cycle, the extent of the electronic rearrangements is smaller compared to previously reported results by our group for Oxy-$Na_{0.67}Li_{0.2}Mn_{0.8}O_2$.[27] Notably, a recent study claimed that a structure at 531 eV in the O K-edge XAS provided evidence for lattice oxygen redox of the kind that has been shown to be caused by formation of trapped molecular oxygen.[18] However, from our RIXS maps for the excitation energy range 530–533, 536 and 545 eV (see Figure S3 in SI) we can clearly rule out that this (potentially detrimental) process is of significance for potentials of up to at least 4.4 V.

Conclusion

In summary, the P3-type Ti^{4+}-substituted $Na_{0.67}Li_{0.2}Ti_{0.15}Mn_{0.65}O_2$ material exhibits a ribbon superstructure, analogous to P3-$Na_{0.67}Li_{0.2}Mn_{0.8}O_2$.[27] Ti^{4+}-substitution enhances the cycling stability, and presents a reversible capacity of 142 mA h g^{-1} after 50 cycles at 10 mA g^{-1} within the voltage range 1.6–4.4 V versus Na/Na^+ and an superior capacity retention compared to Oxy-$Na_{0.67}Li_{0.2}Mn_{0.8}O_2$. *Ex-situ* structural analysis reveals an essentially zero-strain volume change upon initial charge/discharge between 1.8 and 4.4 V versus Na/Na^+ for Oxy-$Na_{0.67}Li_{0.2}Ti_{0.15}Mn_{0.65}O_2$. However, Ti^{4+}-substitution proves to be detrimental to the stability of the anion redox activity, showing a larger voltage hysteresis of 0.18 V over Oxy-$Na_{0.67}Li_{0.2}Mn_{0.8}O_2$ (0.15 V), as a result of loss of superlattice ordering between cations. However, the reversibility of the anion redox behavior is greater than that observed at higher levels of Ti substitution.[26] In Li-ion cells, Oxy-$Na_{0.67}Li_{0.2}Ti_{0.15}Mn_{0.65}O_2$ exhibits promising electrochemical performance, showing a reversible capacity of 162 mA h g^{-1} after 50 cycles (81% capacity retention) between the voltage range 2.0–4.8 V at 50 mA g^{-1} versus Li/Li^+.

Experimental Section

Materials Synthesis

Stoichiometric amounts of sodium carbonate (Na_2CO_3, Fischer Chemistry, ≥99.5%) and lithium carbonate (Li_2CO_3, Fluka, ≥99.0%) were dissolved in deionised water, and added drop-wise to a second solution of manganese(II) acetate tetrahydrate ($Mn(CH_3CO_2)_2 \cdot 4H_2O$, Aldrich, ≥99%) and dihydroxybis(ammonium lactato)titanium(IV) ($([CH_3CH(O^-)CO_2NH_4]_2Ti(OH)_2$) 54.5 wt% in H_2O (Sigma Aldrich) while stirring. The resulting solution was stirred for a further 10 min and the water was removed using a rotary evaporator. The resulting solid was heated to 300 °C at a rate of 6 °C min^{-1} for 12 h and then ground into a fine powder. Oxy-$Na_{0.67}Li_{0.2}Ti_{0.15}Mn_{0.65}O_2$ (also referred to as Oxy-20Li15Ti) was formed by heating the powder to 625 °C at a rate of 5 °C min^{-1} under flowing oxygen (20 cm^3 min^{-1}) and cooling to 50 °C at a rate of 5 °C min^{-1}. Oxy-$Na_{0.67}Li_{0.2}Mn_{0.8}O_2$ (also referred to as Oxy-20Li) was prepared following the same procedure, as detailed elsewhere.[27] The as-synthesized samples were stored in an argon filled glovebox to avoid degradation by atmospheric moisture.

Characterization of as-synthesized materials

Powder X-ray diffraction (PXRD) patterns of as-synthesized materials were recorded on a STOE STADIP diffractometer at room temperature, using Mo $K\alpha_1$ radiation ($\lambda = 0.70930$ Å) in the 2θ range, 4.0–53.0° over 40 mins per scan with a step size of 0.015° and 3267 number of steps and a time per step of 0.92 s in glass capillaries (0.5 mm diameter). Diffraction data were refined using the Rietveld method using Topas Academic V6.[45] Scanning electron microscopy (SEM) and energy dispersive X-ray spectroscopy (EDS) analysis were performed on as-synthesized Oxy-$Na_{0.67}Li_{0.2}Ti_{0.15}Mn_{0.65}O_2$ using a Schottky field-emission gun scanning electron microscopy (FEG-SEM, FEI Scios dualbeam) equipped with an EDAX Octane Plus EDS detector for compositional analysis.

Electrochemical measurements and ex-situ characterization

To examine the electrochemical properties, positive electrodes were prepared using the active material, super C65 carbon and Solef 5130 (modified polyvinylidene fluoride, PVDF) in mass ratios of 75:15:10 in n-methyl-2-pyrrolidone (NMP), which were cast onto aluminum foil using a doctor blade. Electrodes were punched into 13 mm diameter discs before being dried at 80 °C under vacuum. CR2325 coin cells were assembled in an argon filled glovebox consisting of a positive disk electrode, sodium or lithium metal as a counter/reference electrode, and a glass fiber separator (Whatman, GF/F) soaked in electrolyte. For sodium-half cells 1 M $NaPF_6$ in ethylene carbonate/diethyl carbonate (1:1 v/v%, Kishida) or 1 M $NaClO_4$ in propylene carbonate containing 3% fluoroethylene carbonate by weight were used as the electrolyte. As for lithium-half cells, 1.0 M $LiPF_6$ ethylene carbonate/dimethyl carbonate (50/50 v/v, BASF) was used as the electrolyte. Galvanostatic charge/discharge cycling, and voltage scans (linear sweep voltammetry) were collected in a temperature-controlled environment at 30 °C using a Maccor Series 4200 system or Biologic BCS-805 battery cycler.

Electrochemically cycled samples were prepared for *ex-situ* characterization. For *ex-situ* PXRD measurements, working electrodes were prepared by mixing active material and super C65 carbon in mass ratios of 75:25, with no binder and dried at 110 °C under vacuum for 12 h. Swagelok-type cells were assembled as described above, using the electrolyte (1 M $NaClO_4$ in propylene carbonate containing 3% fluoroethylene carbonate by weight). Cells were cycled at 30 °C using a Biologic MacPile II system in galvanostatic mode at 10 mA g^{-1}. Cycled cells were transferred to an argon-filled glovebox and the positive electrodes recovered, washed with dry dimethyl carbonate (DMC, Sigma Aldrich, $\geq$99%) three times and dried under vacuum and samples loaded into glass capillaries (0.5 mm diameter) in an argon filled glovebox. *Ex-situ* PXRD patterns were collected and analyzed as described above.[43] For *ex-situ* soft X-ray absorption spectroscopy (SXAS) and resonant inelastic X-ray scattering (RIXS), CR2325 coin cells were assembled as described above, except that Solupor membranes replaced the glass fiber separator. Manganese L-edge and oxygen K-edge SXAS and RIXS measurements were collected at the C-branch of beamline BL27SU at Spring 8 in Japan.[46] Bulk-sensitive SXAS spectra were obtained in partial fluorescence yield (PFY) mode and inverse partial fluorescence yield (IPFY) mode, the latter is derived by inverting the O K-edge PFY. All SXAS spectra were normalized by the incident intensity, measured by recording the sample drain current and focusing the mirror current using pico-ammeters. Baselines were fitted to the mostly flat regions below any absorption peaks and subsequently subtracted from each spectrum. Further normalization was carried out by setting the low energy region before any absorption peaks to zero and the post-edge region after any absorption features to unity.

Acknowledgements

The authors are grateful for the provision of beam time on BL27SU at Spring 8 (Proposal Number: 2019B1604). We gratefully acknowledge technical support of the Spring 8 user support, particularly beamline scientist K. Tsuruta. This work was supported by the Faraday Institution (grant number FIRG018). The authors gratefully acknowledge support from the Engineering and Physical Sciences Research Council (EPSRC), grants EP/L017008/1, EP/R023751/1 and EP/T019298/1. L. D. gratefully acknowledges financial support from the Swedish Energy Agency (contract 2020-005249). R. Y. and L. M. acknowledge STandLIP for Energy for the financial support.

Conflict of Interest

The authors declare no conflict of interest.

Data Availability Statement

The data that support the findings of this study are available from the corresponding author upon reasonable request.

Keywords: Anion redox chemistry · Layered compounds · Positive electrode material · Sodium · Superstructure

[1] M. S. Whittingham, *Chem. Rev.* **2004**, *104*, 4271–4301.
[2] D. H. Seo, J. Lee, A. Urban, R. Malik, S. Kang, G. Ceder, *Nat. Chem.* **2016**, *8*, 692–697.
[3] K. Luo, M. R. Roberts, R. Hao, N. Guerrini, D. M. Pickup, Y. S. Liu, K. Edström, J. Guo, A. V. Chadwick, L. C. Duda, P. G. Bruce, *Nat. Chem.* **2016**, *8*, 684–691.
[4] E. McCalla, A. S. Prakash, E. Berg, M. Saubanère, A. M. Abakumov, D. Foix, B. Klobes, M.-T. Sougrati, G. Rousse, F. Lepoivre, S. Mariyappan, M.-L. Doublet, D. Gonbeau, P. Novak, G. Van Tendeloo, R. P. Hermann, J.-M. Tarascon, *J. Electrochem. Soc.* **2015**, *162*, A1341–A1351.
[5] M. Sathiya, G. Rousse, K. Ramesha, C. P. Laisa, H. Vezin, M. T. Sougrati, M. L. Doublet, D. Foix, D. Gonbeau, W. Walker, A. S. Prakash, M. Ben Hassine, L. Dupont, J. M. Tarascon, *Nat. Mater.* **2013**, *12*, 827–835.
[6] B. Song, E. Hu, J. Liu, Y. Zhang, X. Q. Yang, J. Nanda, A. Huq, K. Page, *J. Mater. Chem. A* **2019**, *7*, 1491–1498.
[7] X. Bai, M. Sathiya, B. Mendoza-Sánchez, A. Iadecola, J. Vergnet, R. Dedryvère, M. Saubanère, A. M. Abakumov, P. Rozier, J.-M. Tarascon, *Adv. Energy Mater.* **2018**, *8*, 1802379 (1–12).
[8] J. Vinckeviciute, D. A. Kitchaev, A. Van Der Ven, *Chem. Mater.* **2021**, *33*, 1625–1636.
[9] P. Rozier, M. Sathiya, A. R. Paulraj, D. Foix, T. Desaunay, P. L. Taberna, P. Simon, J. M. Tarascon, *Electrochem. Commun.* **2015**, *53*, 29–32.
[10] K. Du, J. Zhu, G. Hu, H. Gao, Y. Li, J. B. Goodenough, *Energy Environ. Sci.* **2016**, *9*, 2575–2577.
[11] A. Tsuchimoto, X. Shi, K. Kawai, B. M. De Boisse, J. Kikkawa, D. Asakura, M. Okubo, A. Yamada, *Nat. Commun.* **2021**, *12*, 1–7.
[12] E. Adamczyk, V. Pralong, *Chem. Mater.* **2017**, *29*, 4645–4648.
[13] B. Mortemard de Boisse, S. ichi Nishimura, E. Watanabe, L. Lander, A. Tsuchimoto, J. Kikkawa, E. Kobayashi, D. Asakura, M. Okubo, A. Yamada, *Adv. Energy Mater.* **2018**, *8*, S1–S7.
[14] Y. Li, X. Wang, Y. Gao, Q. Zhang, G. Tan, Q. Kong, S. Bak, G. Lu, X. Q. Yang, L. Gu, J. Lu, K. Amine, Z. Wang, L. Chen, *Adv. Energy Mater.* **2019**, *9*, 1–9.
[15] B. Song, M. Tang, E. Hu, O. J. Borkiewicz, K. M. Wiaderek, Y. Zhang, N. D. Phillip, X. Liu, Z. Shadike, C. Li, L. Song, Y. Y. Hu, M. Chi, G. M. Veith, X. Q. Yang, J. Liu, J. Nanda, K. Page, A. Huq, *Chem. Mater.* **2019**, *31*, 3756–3765.
[16] Y. Liu, C. Wang, M. Ren, H. Fang, Z. Jiang, F. Li, *J. Energy Chem.* **2021**, *63*, 351–357.
[17] S. F. Linnell, J. Kim, Y. Choi, M. Hirsbrunner, S. Imada, A. Pramanik, F. Cuesta, D. N. Miller, E. Fusco, B. E. Bode, J. T. S. Irvine, L. C. Duda, O. Scanlon, A. R. Armstrong, *J. Mater. Chem. A* **2022**, *10*, 9941–9953.
[18] R. A. House, U. Maitra, M. A. Pérez-Osorio, J. G. Lozano, L. Jin, J. W. Somerville, L. C. Duda, A. Nag, A. Walters, K. J. Zhou, M. R. Roberts, P. G. Bruce, *Nature* **2020**, *577*, 502–508.
[19] J. Ma, S. H. Bo, L. Wu, Y. Zhu, C. P. Grey, P. G. Khalifah, *Chem. Mater.* **2015**, *27*, 2387–2399.
[20] B. Mortemard De Boisse, G. Liu, J. Ma, S. I. Nishimura, S. C. Chung, H. Kiuchi, Y. Harada, J. Kikkawa, Y. Kobayashi, M. Okubo, A. Yamada, *Nat. Commun.* **2016**, *7*, 1–9.
[21] X. Rong, J. Liu, E. Hu, Y. Liu, Y. Wang, J. Wu, X. Yu, K. Page, Y. S. Hu, W. Yang, H. Li, X. Q. Yang, L. Chen, X. Huang, *Joule* **2018**, *2*, 125–140.
[22] E. J. Kim, L. A. Ma, L. C. Duda, D. M. Pickup, A. V. Chadwick, R. Younesi, J. T. S. Irvine, A. Robert Armstrong, *ACS Appl. Energ. Mater.* **2020**, *3*, 184–191.
[23] H. Yoshida, N. Yabuuchi, K. Kubota, I. Ikeuchi, A. Garsuch, M. Schulz-Dobrick, S. Komaba, *Chem. Commun.* **2014**, *50*, 3677–3680.
[24] S. Guo, J. Yi, Y. Sun, H. Zhou, *Energy Environ. Sci.* **2016**, *9*, 2978–3006.
[25] C. Li, C. Zhao, B. Hu, W. Tong, M. Shen, B. Hu, *Chem. Mater.* **2020**, *32*, 1054–1063.
[26] D. Eum, B. Kim, J.-H. Song, H. Park, H.-Y. Jang, S. J. Kim, S.-P. Cho, M. H. Lee, J. H. Heo, J. Park, Y. Ko, S. K. Park, J. Kim, K. Oh, D.-H. Kim, S. J. Kang, K. Kang, *Nat. Mater.* **2022**, *21*, 664–672.
[27] E. J. Kim, P. A. Maughan, E. N. Bassey, R. J. Clément, L. A. Ma, L. C. Duda, D. Sehrawat, R. Younesi, N. Sharma, C. P. Grey, A. R. Armstrong, *Adv. Energy Mater.* **2022**, *12*, 2102325.
[28] E. J. Kim, L. A. Ma, D. M. Pickup, A. V. Chadwick, R. Younesi, P. Maughan, J. T. S. Irvine, A. R. Armstrong, *ACS Appl. Energ. Mater.* **2020**, *3*, 10423–10434.
[29] R. D. Shannon, *Acta Crystallogr.* **1976**, *A32*, 751–767.
[30] X. Rong, E. Hu, Y. Lu, F. Meng, C. Zhao, X. Wang, Q. Zhang, X. Yu, L. Gu, Y. S. Hu, H. Li, X. Huang, X. Q. Yang, C. Delmas, L. Chen, *Joule* **2019**, *3*, 503–517.
[31] X. Cao, X. Li, Y. Qiao, M. Jia, F. Qiu, Y. He, P. He, H. Zhou, *ACS Energy Lett.* **2019**, *4*, 2409–2417.

[32] C. Zhao, Z. Yao, J. Wang, L. Yaxiang, X. Bai, A. Aspuru-Guzik, L. Chen, Y.-S. Hu, *Chem* **2019**, *5*, 2913–2925.
[33] A. R. Armstrong, P. G. Bruce, *J. Mater. Chem.* **2005**, *15*, 218–224.
[34] A. R. Armstrong, P. G. Bruce, *Electrochem. Solid-State Lett.* **2004**, *7*, 3–6.
[35] J. M. Paulsen, J. R. Dahn, *Solid* **1999**, *126*, 3–24.
[36] A. D. Robertson, P. G. Bruce, *Chem. Mater.* **2003**, *15*, 1984–1992.
[37] A. R. Armstrong, N. Dupre, A. J. Paterson, C. P. Grey, P. G. Bruce, *Chem. Mater.* **2004**, *16*, 3106–3118.
[38] A. R. Armstrong, A. J. Paterson, N. Dupré, C. P. Grey, P. G. Bruce, *Chem. Mater.* **2007**, *19*, 1016–1023.
[39] K. Takada, H. Sakurai, E. Takayama-muromachi, F. Izumi, R. A. Dilanian, S. T, *Nature* **2003**, *422*, 53–55.
[40] M. Kalapsazova, G. F. Ortiz, J. L. Tirado, O. Dolotko, E. Zhecheva, D. Nihtianova, L. Mihaylov, R. Stoyanova, *ChemPlusChem* **2015**, *80*, 1642–1656.
[41] Y. N. Zhou, P. F. Wang, X. D. Zhang, L. B. Huang, W. P. Wang, Y. X. Yin, S. Xu, Y. G. Guo, *ACS Appl. Mater. Interfaces* **2019**, *11*, S1–S15.
[42] D. Asakura, E. Hosono, Y. Nanba, H. Zhou, J. Okabayashi, C. Ban, P. A. Glans, J. Guo, T. Mizokawa, G. Chen, A. J. Achkar, D. G. Hawthron, T. Z. Regier, H. Wadati, *AIP Adv.* **2016**, *6*, 035105–1–8.
[43] U. Maitra, R. A. House, J. W. Somerville, N. Tapia-Ruiz, J. G. Lozano, N. Guerrini, R. Hao, K. Luo, L. Jin, M. A. Pérez-Osorio, F. Massel, D. M. Pickup, S. Ramos, X. Lu, D. E. McNally, A. V. Chadwick, F. Giustino, T. Schmitt, L. C. Duda, M. R. Roberts, P. G. Bruce, *Nat. Chem.* **2018**, *10*, 288–295.
[44] S. F. Linnell, M. Hirsbrunner, S. Imada, G. Cibin, A. B. Naden, A. V. Chadwick, J. T. S. Irvine, L. C. Duda, A. R. Armstrong, *ChemElectroChem* **2022**, *9*, e202200240.
[45] A. A. Coelho, *J. Appl. Crystallogr.* **2018**, *51*, 210–218.
[46] H. Ohashi, E. Ishiguro, Y. Tamenori, H. Kishimoto, M. Tanaka, M. Irie, T. Tanaka, T. Ishikawa, *Nucl. Instrum. Methods Phys. Res. Sect. A* **2001**, *467–468*, 529–532.

Manuscript received: September 7, 2022
Revised manuscript received: September 19, 2022
Accepted manuscript online: September 19, 2022